Molecular basis of multistep voltage activation in plant two-pore channel 1

Miles Sasha Dickinson[a,b,1], Jinping Lu[c,1], Meghna Gupta[a], Irene Marten[c], Rainer Hedrich[c,2], and Robert M. Stroud[a,2]

[a]Department of Biochemistry and Biophysics, University of California, San Francisco, CA 94143; [b]Chemistry and Chemical Biology Graduate Program, University of California, San Francisco, CA 94143; and [c]Department of Molecular Plant Physiology and Biophysics, University of Würzburg, D-97082 Würzburg, Germany

Voltage-gated ion channels confer excitability to biological membranes, initiating and propagating electrical signals across large distances on short timescales. Membrane excitation requires channels that respond to changes in electric field and couple the transmembrane voltage to gating of a central pore. To address the mechanism of this process in a voltage-gated ion channel, we determined structures of the plant two-pore channel 1 at different stages along its activation coordinate. These high-resolution structures of activation intermediates, when compared with the resting-state structure, portray a mechanism in which the voltage-sensing domain undergoes dilation and in-membrane plane rotation about the gating charge–bearing helix, followed by charge translocation across the charge transfer seal. These structures, in concert with patch-clamp electrophysiology, show that residues in the pore mouth sense inhibitory Ca^{2+} and are allosterically coupled to the voltage sensor. These conformational changes provide insight into the mechanism of voltage-sensor domain activation in which activation occurs vectorially over a series of elementary steps.

cryoelectron microscopy | atomic structure | two-pore channel | electrophysiology | calcium-gated channel

Voltage-gated ion channels (VGICs) use voltage-sensing domains (VSDs) to sense changes in electrical potential across biological membranes (1, 2). VSDs are composed of a four-helix bundle, in which one helix carries charged residues that move in response to changes in transmembrane electric field (3, 4). VSDs usually adopt a "resting state" when the membrane is at "resting potential": ~ -80 mV for animal and ~ -150 mV for plant plasma membranes (5). In comparison, much lower resting membrane voltages are set for intracellular endo-membranes: ~ -30 mV across the plant vacuole (6) and mammalian lysosome (7). As the membrane potential vanishes during depolarization, so does the downward electrostatic force on the cationic side chains causing them to relax toward the outside of the membrane across a hydrophobic constriction site (HCS) or hydrophobic seal (8). This conformational change is conveyed to the central pore, formed by four pore domains in a quasi-fourfold arrangement, which dilates to allow the diffusion of ions down their electrochemical gradients. The exact nature of the conformational change in VSDs has been the subject of decades of biophysical investigation (9–12), though to this date, only a few structural examples exist of voltage sensors in resting or multiple conformations (13–18).

Two-pore channels (TPCs) are defined by their two tandem *Shaker*-like cassette subunits in a single polypeptide chain, which dimerize to form a C2-symmetric channel with four subunits and 24 (4 × 6) transmembrane helices (19–21). There are three TPC channels, TPC1, 2, and 3, each with different voltage or ligand gating and ion selectivity. Among the voltage-gated TPCs (all except lipid-gated TPC2), only the second VSD (VSD2) is electrically active (18, 22–24), while VSD1 is insensitive to voltage changes and is likely static under all changes in potential.

In plants, the vacuole comprises up to 90% of the plant cell volume and provides for a dynamic storage organelle that, in addition to metabolites, is a repository for ions including Ca^{2+}. TPC1 channels confer excitability to this intracellular organelle (25) and, unlike other TPCs, are calcium regulated: external Ca^{2+} (in the vacuolar lumen) inhibits the channel by binding to multiple luminal sites, while cytosolic Ca^{2+} is required to open the channel by binding to EF hands, although the exact mechanism by which this activation occurs is unknown (22). These electrical properties allowed our group and Youxing Jiang's group to determine the first structure of an electrically resting VGIC by cocrystallizing the channel with 1 mM Ca^{2+}, which maintains the VSD in a resting configuration at 0 mV potential (16, 22).

Previously (17), we used a gain-of-function mutant of AtTPC1 with three luminal Ca^{2+}-binding acidic residues on VSD2 neutralized (D240N/D454N/E528N) termed AtTPC1$_{DDE}$ (abbreviated here as DDE) to visualize channel activation at the level of atomic structure, but we were unable to sufficiently resolve details of the electrically active VSD2 due to structural heterogeneity. In addition, the intracellular activation gate remained closed. We now present multiple structures of intermediately activated states of AtTPC1 determined by extensive image processing. In order to visualize such states, we

Significance

Despite decades of biophysical and structural research, little is understood about how voltage-gated ion channels (VGICs) activate during membrane depolarization, and less is known about how VGICs can be modulated by lipids and other ligands. We identify multiple functional states of the voltage- and Ca^{2+}-gated ion channel TPC1 from *Arabidopsis thaliana* (AtTPC1), which confers electrical excitability to the plant vacuole. Here, we show how a voltage-sensing domain (VSD) functions during electrical activation and the mechanism of inhibition by vacuolar Ca^{2+}. We show that the VSD undergoes large-scale, domain-wide structural changes during activation that involves Ca^{2+}-dependent in-membrane plane rotation, subsequent charge transfer, and a Ca^{2+}-dependent gate in the pore mouth that is allosterically coupled to the VSD.

modulated the channel's luminal Ca^{2+} sensitivity using a well-studied gain-of-function single-point mutant, D454N (*fou2*), and also the triple mutant DDE for comparison. *fou2* is known to desensitize the channel to inhibitory, external (luminal) calcium ions (26, 27). Mutations in D454 and closely related luminal Ca^{2+}-binding carboxyls to alanine D240A, D454A, E528A (termed $AtTPC1\Delta Ca_i$) were previously shown to effectively attenuate the Ca^{2+}-induced shift of the voltage activation threshold of AtTPC1 to depolarizing potentials at high luminal Ca^{2+} (28).

The *fou2* and DDE mutations lie in the coordination sphere of the inhibitory Ca^{2+} site on the luminal side of the VSD2–pore interface formed by D454, D240, and E528. The D454N mutation in the *fou2* channel enhances the defense capacity of plants against fungal or herbivore attack due to increased production of the wounding hormone jasmonate (29). These effects on plant performance and defense are probably due to short circuiting of the vacuolar membrane (26, 27, 30) in which TPC1 has increased open probability at resting potential. Compared to wild-type (WT) TPC1, the activation threshold in the *fou2* channel is shifted to more negatively polarized potentials and also has significantly lower sensitivity to inhibitory Ca^{2+} in addition to exhibiting faster activation kinetics than its WT counterpart that was originally named the "slow vacuolar" (SV) channel due to its slow conductance onset (20, 21, 30). Therefore, D454N confers more than just reduced sensitivity to external Ca^{2+} but intrinsic hyperactivity as well. Our structures of these AtTPC1 mutants attempt to explain how the voltage sensor functions during electrical activation and how exactly luminal Ca^{2+} affects this process.

Results

Experimental Design of Cryoelectron Microscopy and Electrophysiology Experiments.
In order to examine the role of inhibitory Ca^{2+} in the electrical activation process of AtTPC1, we determined cryoelectron microscopy (cryoEM) structures of mutants that perturb luminal Ca^{2+} binding and performed patch-clamp electrophysiology on plant vacuole–bound TPC1 channels. We prepared mutant channels for single-particle analysis by vacuolar expression in *Saccharomyces cerevisiae* followed by solubilization using the gentle detergent glycodiosgenin (*SI Appendix*, Fig. S2). The channels were then imaged and reconstructed to near-atomic resolutions of ~3 Å (Fig. 1*C*). To test whether WT and mutant TPC1 channels generated were properly targeted in the plant cell, leaf protoplasts (mesophyll cells with removed cell wall) from *Arabidopsis* plants (Fig. 1*A*) were transiently transformed with carboxyl-terminal GFP-tagged versions of the plant two-pore channel TPC1. Upon selective osmotic disruption of the plasma membrane (31), the green fluorescence of TPC1-GFP expressing vacuoles (Fig. 1*B* and *SI Appendix*, Fig. S1*A*) is visible and their vacuolar membrane accessible for patch-clamp electrophysiology (see Fig. 4).

D454 Controls Compactness of the VSD.
In the presence of 1 mM Ca^{2+}, the D454N channel still binds Ca^{2+} via the two other carboxylate residues that remain in the WT chelation site: D240 from the N-terminal pore domain and E528 from the gating charge–bearing S10 helix (Fig. 2*A*). Loss of the negatively charged residue D454 on S7 of VSD2 causes the helix S7 to move away from the charge transfer center (CTC), and subsequent shifting of S8 and S9 causes dilation of the VSD (Fig. 2*A*). This subtle structural rearrangement results in a slightly more "relaxed" four-helix bundle, indicating that the luminal Ca^{2+} site controls domain constriction. This less sterically hindered conformation of the VSD may explain the mutant's fast activation by decreasing resistance of the charge transfer pathway. Accompanying this conformational change is a full 180° rotation (relative

to WT) of the luminal residues on S10 due to a 3_{10} to α-helix transition, causing R531 (one of the voltage-sensing arginines) to move from interacting with negatively charged E511 to E468. Despite these differences, the gating charges (R3-R5 in the *Shaker* convention) located along the S10 helix are still in the "down state," overlaying almost exactly with those in the WT Ca^{2+}-bound crystal structure (Fig. 2*A*). Therefore, D454N does not ablate inhibition by external Ca^{2+} but rather primes the VSD for activation by unlocking S7 from the VSD–pore interface.

The VSD Ca^{2+} Site Forms a Hinge between the Pore and VSD.
Removal of Ca^{2+} from the D454N channel renders the VSD much more dynamic. In the presence of the calcium chelator EDTA (ethylenediaminetetraacetic acid disodium salt dihydrate), VSD2 is highly mobile and is barely visible in initial reconstructions (with and without the imposition of C2 symmetry), despite the fact that the rest of the channel is resolved to ~3 Å resolution. C2 symmetry expansion followed by three-dimensional (3D) variability analysis in cryoSPARC revealed that VSD2 undergoes substantial lateral movement in the membrane plane, rotating approximately as a rigid body about the gating charge–bearing helix S10, explaining why the domain is poorly resolved. In order to separate these states, we performed iterative rounds of masked "skip-align" classification on VSD2 using the C2 symmetry–expanded particle stack, which recovered three discrete states of the voltage sensor, termed states I through III (Fig. 2*B*). These particle sets were then subjected to gold-standard or resolution-limited refinement in RELION and cisTEM, respectively. State I was refined to the highest resolution (<3 Å resolution) and is apparently identical to the D454N, external Ca^{2+}-bound (resting state) structure. State II (at ~3 to 4 Å resolution) and state III (at ~8 Å resolution) exhibit significant conformational changes from the Ca^{2+}-bound structure, in which the VSD2 helices have rotationally shifted by ~10 Å at the outermost region. In state II, the gating charges have moved ~7 Å upwards by approximately one helical turn (i.e., one "click") so that one charge is transferred across the HCS formed by Y475 (Fig. 2*C*). Interestingly, R543 (R5 in the *Shaker* convention) has rotated out of the four-helix bundle to point more toward the pore (Fig. 2*C*). This demonstrates that the gating charges translocate upwards in this activated state, in contrast to our previously suggested mechanism (17), although dynamics in the entire VSD do seem to play an integral part in activation. These dynamics may explain, in part, why sufficiently high resolution in VSD2 was not previously achievable. S10 in state II has also moved subtly (~5 Å) from its position in state I, and Y475 from S8 (that forms the hydrophobic seal of the CTC, termed HCS) moves by ~5 Å in the membrane plane, probably to prevent a steric clash with R4 and R5 during charge translocation (Fig. 2*C*). Accompanying the movement of S10 is a small upward shift in the last two helical turns of the S10–S11 linker (i.e., the domain II equivalent of the S4–S5 linker). This shifts the linker away from the gate-forming S6 helix, clearing a path for dilation of the intracellular activation gate. As intracellular Ca^{2+} is necessary for channel activation, it is conceivable that an accompanying shift in S6 to open the gate only occurs when the EF hands are Ca^{2+} loaded, although the exact mechanism of how this would occur is unclear. These data suggest that the electrical activation process in AtTPC1 differs from all other structurally characterized VGIC mechanisms: large-scale conformational changes in the VSD precede charge translocation.

The DDE Ca^{2+} Channel VSD Is Apparently Identical to State II of D454N/EDTA and Retains a Closed Pore.
In order to compare these results with our previous observations from saposin-solubilized DDE (17), we determined a structure of the DDE channel solubilized in glycodiosgenin, in the presence of 1 mM Ca^{2+} (*SI*
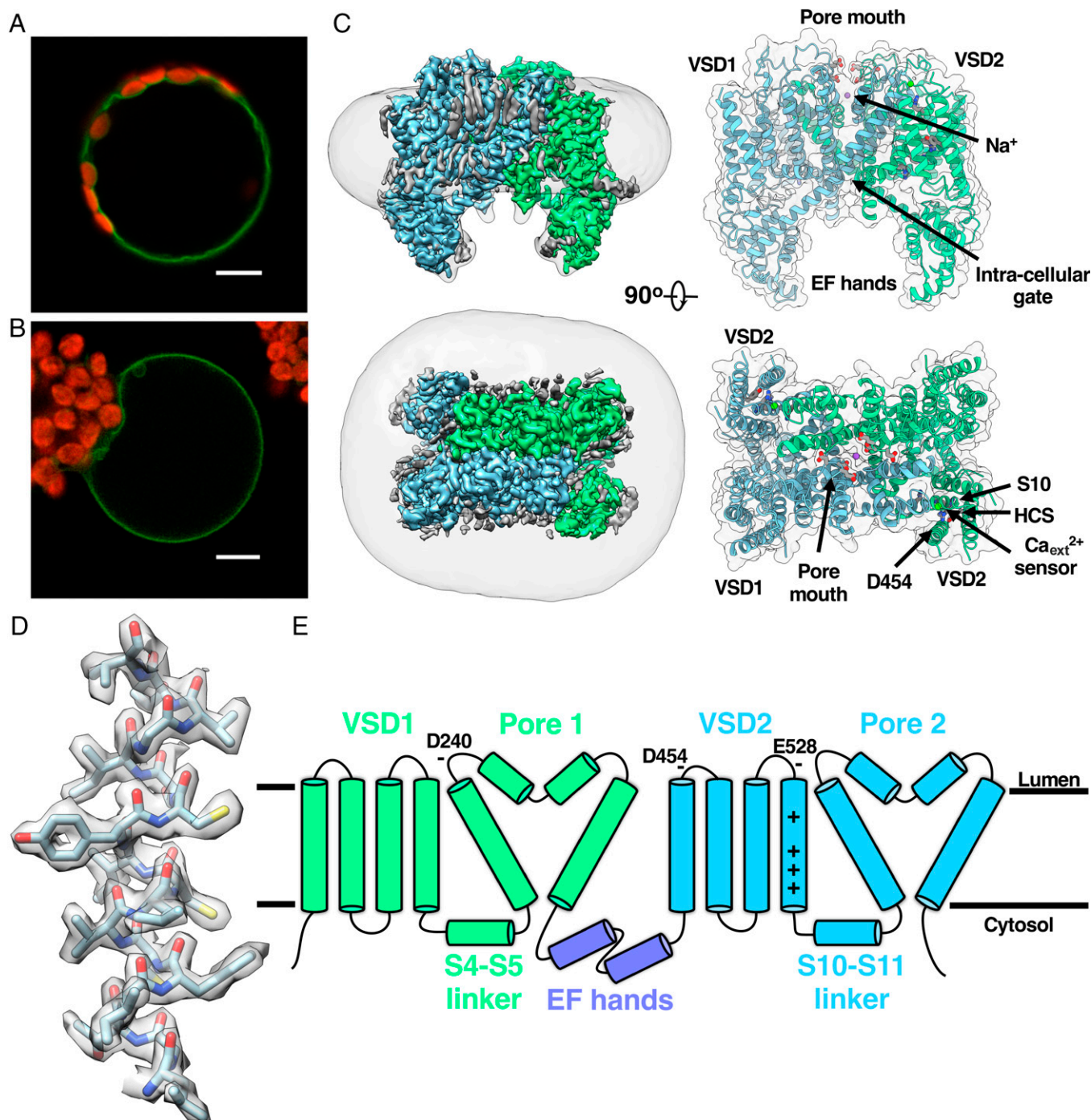
Fig. 1. CryoEM structure of the vacuolar two-pore channel 1 D454N at near-atomic resolution. (*A*) Confocal fluorescent image of an *Arabidopsis* leaf protoplast released from the TPC1 loss-of-function mutant *tpc1-2* expressing a TPC1-GFP construct. (*B*) Confocal fluorescent image of the vacuole liberated by selective hypoosmotic shock from a protoplast depicted in *A*. In *A* and *B*, red fluorescence results from chlorophyll autofluorescence of chloroplasts (Scale bar, 10 μm.) (*C*) Orthogonal views of the luminal Ca^{2+}-bound, unsharpened Coulomb potential map, colored by subunit, along with the atomic model annotated with functionally relevant residues from the VSD2 and pore. Please note that Ca^{2+} on the EF hands is not shown. Ca_{ext}^{2+} sensor = luminal, inhibitory Ca^{2+} sensor. A low-pass filtered map is shown to approximate the boundaries of the detergent micelle. (*D*) Atomic detail in the potential map obtained after density modification, showing the quality of the fitted structure. (*E*) One-dimensional schematic of the domain arrangement of the AtTPC1 polypeptide.

Appendix, Fig. S5). In this triple-mutant channel, D454, D240, and E528 (of the VSD2 Ca^{2+} coordination sphere) have been substituted with alanine as opposed to their cognate amides. As in our D454N EDTA dataset, multiple VSD states were recovered from 3D classification in which the S7-S9 helices have undergone a substantial in-membrane plane rotation about S10, which we compare to the aforementioned states I and II

recovered from the D454N EDTA dataset (*SI Appendix,* Fig. S5). We observe a correlation between resolvability of the EF hands and lateral shift of the VSD, wherein the state I EF-hand domain is well resolved, whereas it is disordered in the state II conformation. It is possible that EF hand–VSD contacts are broken during VSD shifting such that the EF hands are no longer rigid. Instability in the EF hands may be a prerequisite for stochastic opening
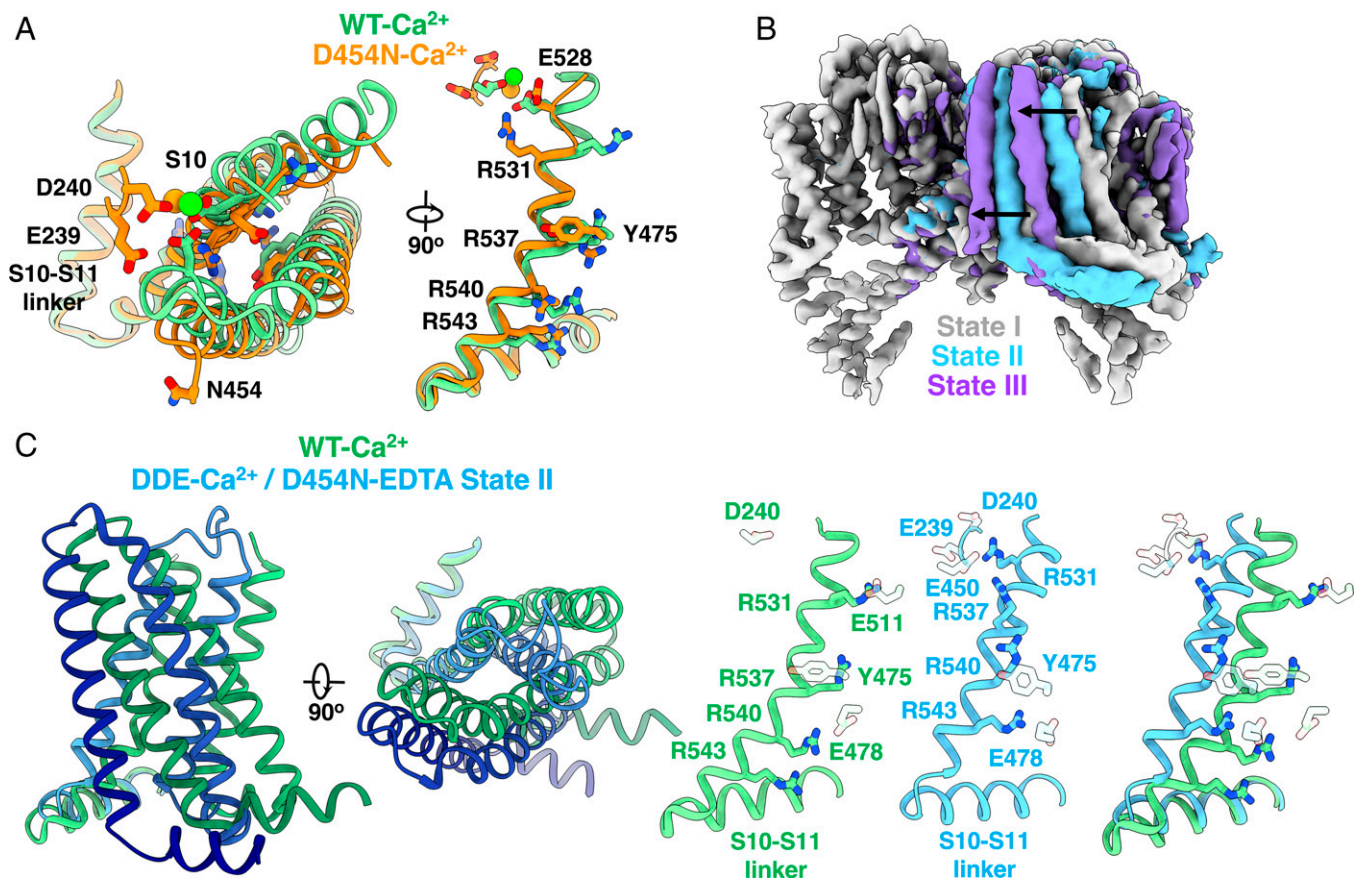
Dickinson et al.
Molecular basis of multistep voltage activation in plant two-pore channel 1

PNAS | 3 of 10
https://doi.org/10.1073/pnas.2110936119

Fig. 2. Conformational flexibility in VSD2 and charge transfer during voltage activation. (*A*) Structural comparison of VSD2 between the WT crystal structure (PDB: 5DQQ) and D454N-Ca^{2+}, showing dilation of the four-helix bundle and HCS, loss of 3_{10} helicity at the luminal side of S10, and remodeling of the Ca$_{ext}$$^{2+}$ site. Ca^{2+} atoms are shown as green and orange spheres. (*B*) Three conformations of VSD2 are observed from 3D classification of the D454N-EDTA dataset, shown here as the unsharpened electrostatic potential maps from the classification job. State I (in gray) is most similar to the Ca^{2+} dataset, and state III (in purple) is most distinct with quasi-C4 symmetry. (*C*) Charge translocation in S10 is defined by a combination of upwards translation and helical screw type motion, accompanied by retraction of the hydrophobic constriction site, Y475 (HCS). On the left are orthogonal views of VSD2. On the right is a detailed comparison of the charge transfer centers in the resting (green) and partially activated (blue) states.

of the intracellular activation gate, although it is still unclear why our DDE Ca^{2+} structures retain a closed gate.

We conclude that D454 controls internal compactness of the VSD (as concluded from our D454N Ca^{2+} structure) and that D240 (from the pore domain) and E528 (from VSD2) stabilize the Ca^{2+}-dependent tether between VSD2 and the pore—thus, the Ca^{2+}-binding site at this VSD2–pore interface forms a "hinge," the angle at which is determined by the presence of Ca^{2+}. In the presence of luminal, inhibitory Ca^{2+} (termed Ca$_{ext}$$^{2+}$), the VSD is poised inwards, resulting in a more C2 rectangular channel locked in place by an interdomain chelate. Removal of the Ca$_{ext}$$^{2+}$ allows the VSD to move in plane, sampling multiple discrete states. When in the outwardly poised state (i.e., the channel is more quasi-C4 symmetric) and the membrane potential has sufficiently depolarized, the S10 helix can activate, during which the gating charges translocate upwards to access extracellular solvent (Fig. 2C). Crystal structures of the bacterial Na$^+$ channels Na$_V$Rh and Na$_V$Ab show large differences in orientations between the VSD and pore (32–35). Furthermore, the angle between the VSD and pore domains of TPC3 (18) and murine TPC1 (36) may suggest that VSD mobility across the two-pore channel family is an essential component of channel activation and that electromechanical coupling may consist of more complex motions than the push/pull mediated by the S4-S5 (or S10-S11 in VSD2) linker.

While all animal TPCs are Na$^+$-selective, plant TPC1 conducts K$^+$, Na$^+$, and Ca^{2+}, and this lack of cation discretion is

conferred by its quasi-fourfold selectivity filter, with two residues, M629 and G630, from the second pore domain (filter II) that abolish Na$^+$ selectivity (22, 23, 28, 35) (Fig. 3 *A* and *B*). Our D454N Ca^{2+} structure, at ~2.5 Å resolution, reveals a detailed arrangement of pore densities that we assign to waters around a single metal bound in the selectivity filter, demonstrating exactly how permeant ions interact with the conduction pathway (Fig. 3 *C* and *D*). The pore domain of the mutant channel has completely reorganized with respect to WT, making and breaking contacts relative to the crystal structure of WT AtTPC1. In comparison to our WT TPC1 structure (Protein Data Bank [PDB]: 5DQQ), N631 from filter II has rotated 90° to avoid interacting with its symmetry mate across the pore (Fig. 3B). The hydroxyl of Y608 is repositioned 11 Å to contact the water network around the sodium ion, and D606 is moved by 4 Å into the central water network. In the WT crystal structure, the twofold symmetry-related E605 pair forms the constriction point of the pore mouth situated above the selectivity filter and bound an Yb^{2+} ion (a Ca^{2+} mimetic used for phase determination). In D454N, E605 is removed from the conduction pathway, significantly altering the topology and electrostatics of the mouth (Fig. 3 *B* and *E*).

Interestingly, F611 also moves to displace another Ca^{2+} ion observed in the WT crystal structure between N612 and N625. Multiple unmapped inhibitory Ca^{2+} sites exist in the pore domain of AtTPC1 (20), so these mutant-driven rearrangements may alleviate Ca^{2+} inhibition at the pore. In summary,
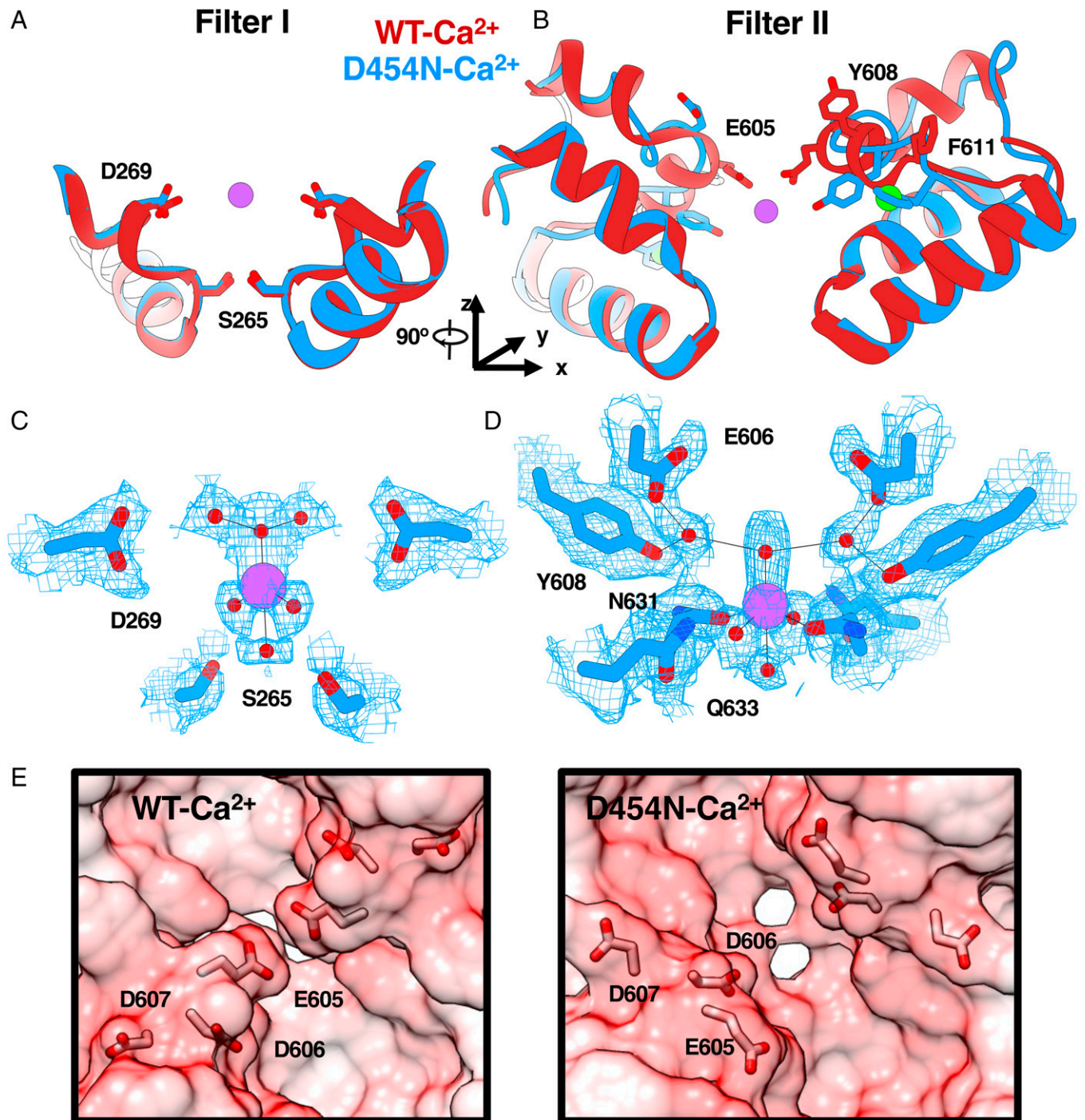
Fig. 3. Conformational changes in the pore domain between AtTPC1 WT and D454N. (A) Overlay of WT AtTPC1 (red, PDB: 5DQQ) and D454N-Ca^{2+} (blue) showing no perturbations of side chains of filter I due to the mutation. The channel axes are shown where z is coincident with the pore and perpendicular to the plane of the membrane (xy-plane). (B) Large conformational changes in the metal- and water-binding pore residues from filter II along with exclusion of a proximal Ca^{2+} ion by F611. (C) Density-modified potential map zoned 2 Å around atoms of interest showing hydration around the bound metal and interactions with filter I. (D) Same as C but from the perspective of filter II. (E) Coulombic surface representation of the pore mouth of WT (*Left*) and D454N (*Right*) showing how rearrangements in the three acidic residues 605 to 607 alter the topology of the region. The viewing direction is in parallel with the pore axis.

we conclude that the Ca^{2+}-dependent positioning of D454 is allosterically coupled to the pore and that the insensitivity of *fou2* (D454N) to luminal Ca^{2+} is manifest in three locations. Therefore, the diminished sensitivity to luminal, inhibitory Ca^{2+} in the *fou2* channel can be explained by these conformational changes, which clearly show that Ca^{2+}-binding sites are

remodeled to exclude Ca^{2+} at multiple sites across the channel's luminal face.

Since the TPC1 channel is a nonselective cation channel, the ion we see in the selectivity filter could be either Na$^+$ or Ca^{2+} (K$^+$ is absent from the buffer). Despite the buffer consisting of a 200-fold excess of Na$^+$ (200 mM versus 1 mM Ca^{2+}), we

Dickinson et al.
Molecular basis of multistep voltage activation in plant two-pore channel 1

PNAS | 5 of 10
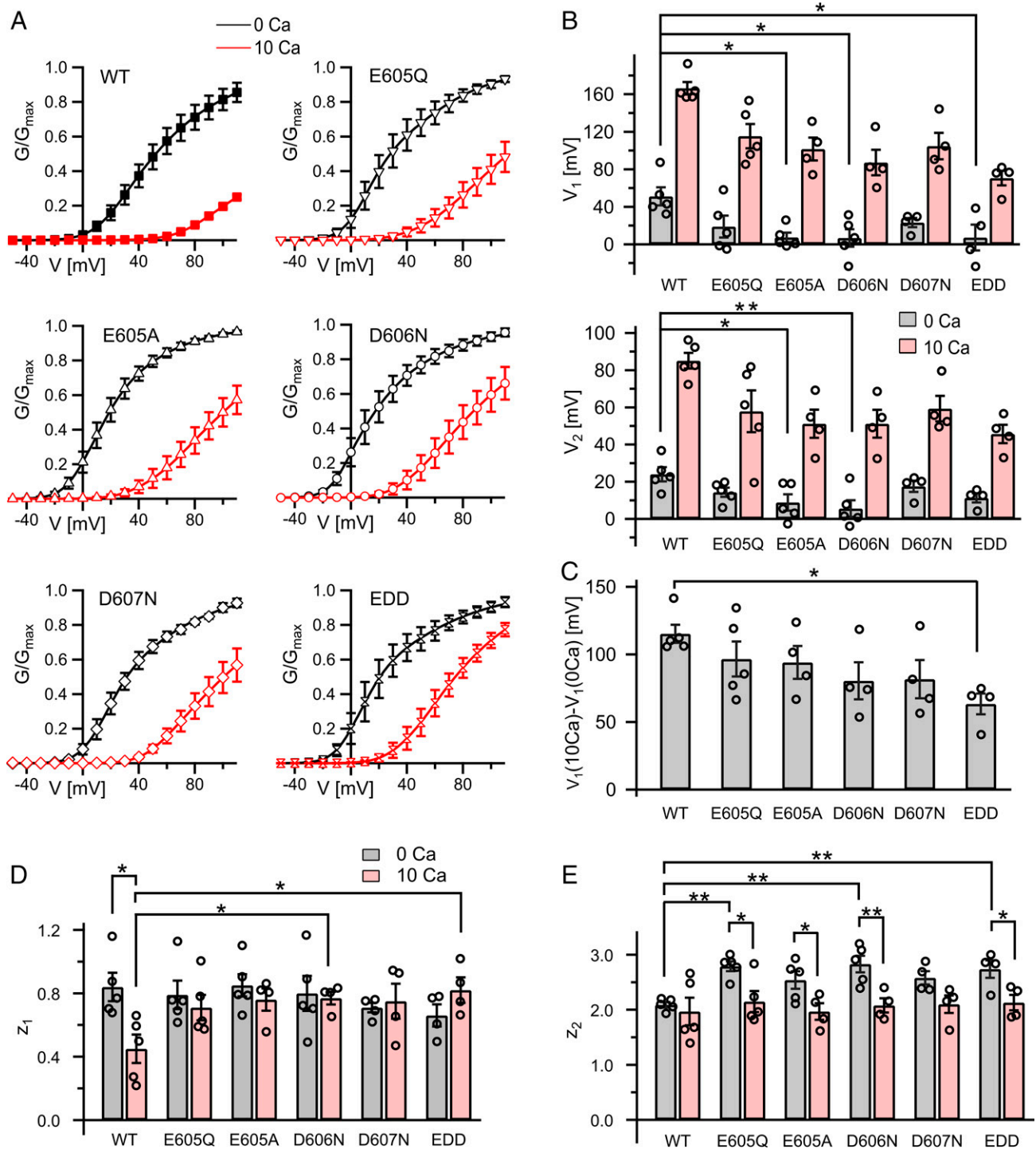https://doi.org/10.1073/pnas.2110936119

Fig. 4. The pore mouth operates a luminal Ca^{2+} sensor functionally coupled to the voltage sensor. (*A*) Normalized conductance–voltage plots [$G/G_{max}(V)$] of WT and pore-mouth mutants in the presence (red symbols and line, 10 mM Ca^{2+}) and absence (black symbols and line) of luminal Ca^{2+}. Symbols represent means ± SE, and solid lines provide the best fits of the G(V) plots to a double Boltzmann function. (*B*) Half-activation voltages V_1 and V_2 given as means ± SE in the presence of 0 and 10 mM Ca^{2+} in the vacuole lumen. $V_{1/2}$ values were derived from the double Boltzmann fits of the G(V) plots shown in *A*. Significant differences were only analyzed for $V_{1/2}$ values under luminal Ca^{2+}-free conditions with one-way ANOVA followed by Dunnett's post hoc comparison test. (*C*) Changes in V_1 values upon a rise in luminal Ca^{2+} from 0 to 10 mM. Significant differences tested with one-way ANOVA followed by Dunnett's post hoc comparison test. Note, Ca^{2+}-induced changes in V_2 values for all channel variants are summarized in *SI Appendix*, Table S1. (*D* and *E*) The number of apparent gating charges z_1 and z_2 (means ± SE) at 0 and 10 mM luminal Ca^{2+} derived from the double Boltzmann fits of the G(V) plots shown in *A*. Significant differences in the gating charges between the WT and the channel mutants were analyzed for each Ca^{2+} condition with one-way ANOVA followed by Dunnett's post hoc comparison test. Significance of Ca^{2+}-induced changes in $z_{1/2}$ values were tested with Student's *t* test. Significant differences between tested groups in *B–E* are indicated by asterisks (*$P < 0.05$ and **$P < 0.01$). In the bar charts (*B–E*), open black circles represent individual data points. In *A–E*, the number of experiments performed on individual vacuoles per channel variant was $n = 5$ for WT, E605Q, E605A, and D606N and $n = 4$ for D607N and EDD under luminal Ca^{2+}-free conditions. For 10 mM luminal Ca^{2+}, the number of experiments was $n = 5$ for WT and E605Q and $n = 4$ for E605A, D606N, D607N, and EDD.
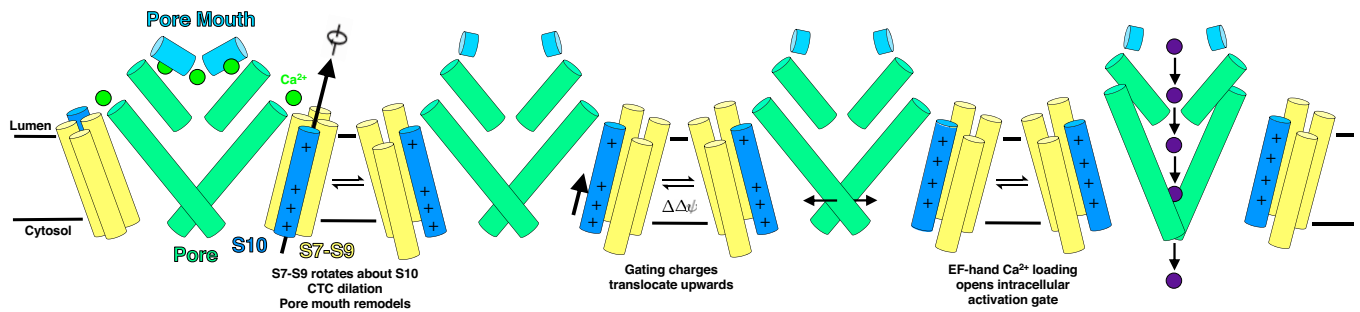
6 of 10 | PNAS
https://doi.org/10.1073/pnas.2110936119

Dickinson et al.
Molecular basis of multistep voltage activation in plant two-pore channel 1

Fig. 5. Proposed mechanism of AtTPC1 voltage activation: In the presence of luminal Ca^{2+} (Ca_{ext}^{2+}), the VSD is compact and the gating charges are in the "down" position. Removal of luminal Ca^{2+} dilates the CTC and S7-S9 move rotationally around S10. This flexibility in the VSD is coupled to conformational change in the pore mouth that transitions between a Ca^{2+} binding–competent and –incompetent state. If the membrane potential is sufficiently depolarized, the gating charges will translocate upwards into their electrically active state. While in the electrically activated state, the intracellular activation gate can open when the cytosolic EF hands are loaded with Ca^{2+}.

cannot faithfully assign an identity to the observed metal in the filter, as we do not know their respective affinities, the putative coordination geometry is favorable for either ion (1, 37–39), and the ionic radii of Na^+ and Ca^{2+} (1.16 Å and 1.14 Å, respectively) are almost identical. The amide carbonyl to metal distance is 2.3 Å, and the equatorial water to metal distance is 2.5 Å. We used the CheckMyMetal server (40) to validate the consistency of ions in this position. The coordination geometry is almost octahedral, though the lower axial water to ion distance is 2.9 Å.

The Pore Mouth Influences Voltage and Luminal Ca^{2+} Sensing. The cryoEM structure of *fou2* shows rearrangements of luminal pore residues (termed the "pore mouth"); the carboxylate residues E605, D606, and D607 are repositioned and so cause an apparent loss of the luminal Ca^{2+} coordination site on the pore axis (Fig. 3). Therefore, in order to determine what functional effect the pore mouth has on TPC1 channel activation, we made substitutions at those positions and transiently transformed protoplasts of the TPC1 loss-of-function mutant *tpc1-2* with individual single and triple TPC1 mutant channels. Patch-clamp measurements with isolated TPC1-transformed vacuoles were performed in the whole-vacuole configuration (*SI Appendix*, Fig. S1*A*). Typical macroscopic, outward-rectifying TPC1 currents were recorded in response to membrane depolarization (*SI Appendix*, Fig. S1 *B* and *C*). Raising the luminal Ca^{2+} concentration from 0 to 10 mM affected both ion channel current amplitude (*SI Appendix*, Fig. S1 *B* and *C*) and voltage-dependent properties (Fig. 4). As a proxy for the latter, we displayed the voltage-dependent relative open-channel probability (Fig. 4*A*). To our surprise, mutating the negatively charged residues impacted channel function in three ways. First, in the absence of luminal Ca^{2+}, the open probability of the single-mutant channels (E605A and D606N) and the triple mutant EDD shifted significantly toward more negatively polarized membrane potentials (Fig. 4*B*). Second, while the channel variants (i.e., mutants and WT) transferred a comparable number of equivalent gating charges z_1, more gating charges z_2 were moved in the channel mutants E605Q/A, D606N, and triple-mutant EDD than in WT during activation under luminal Ca^{2+}-free condition (Fig. 4 *D* and *E*). An increase in luminal Ca^{2+} differentially affected the gating-charge movement during channel activation. The number of gating charges z_1 decreased in the WT but not in the mutant channels (Fig. 4*D*). Instead, all mutant channels except D607N transferred fewer gating charges z_2 at high luminal Ca^{2+} than at 0 mM Ca^{2+}, whereas a similar number of gating charges z_2 was detected for WT under these two Ca^{2+} conditions (Fig. 4*E*). Third, neutralization of all three amino acids together (EDD) further reduced the susceptibility to the inhibitory luminal gating modulator Ca^{2+} (Fig.

4*C*). Taken together, these results suggest that the negatively charged cluster at the external entrance to the pore (605 to 607) are involved in channel gating as a Ca^{2+} sensor.

Discussion

We used cryoEM to explore the electrical activation of a Ca^{2+}-regulated VGIC. Our structures show that the voltage sensor undergoes a number of discrete steps along its activation coordinate, including dilation, in-plane rotation, and finally, charge translocation (Fig. 5). Furthermore, we show that the VSDs are coupled to a luminal Ca^{2+} sensor within the conduction pathway, termed the pore mouth, and that the conformational changes we observe in that region are functionally relevant. This gating at the pore mouth functions in addition to steric gating at the canonical intracellular activation gate. While we describe herein the mechanism for electrical activation and luminal Ca^{2+} inhibition, we are currently unable to determine how the EF hands ultimately bind cytosolic Ca^{2+} to open the intracellular activation gate.

The *fou2* channel has previously been shown to have faster activation kinetics and altered voltage- and calcium-dependent gating compared to the WT channel (26, 29). Our data here allow us to propose two reasons for these observations. First, dilation of the VSD lowers the energetic barrier to gating-charge translocation across the HCS, resulting in the observed faster voltage-dependent activation. Second, significant conformational changes in the external mouth of the pore may decrease the resistance of the conduction pathway, likely through steric effects and complex interactions with the extracellular hydration network. These conformational changes in the pore mouth reflect allosteric communication from the VSD that are apparently not conveyed through the S10–S11 linker, since it remains unchanged structurally, but rather through subtle rearrangements near the VSD2 Ca^{2+} site. Therefore, the D454 position, given its placement between VSD2 and the central pore, represents an important regulatory site in the luminal face of the channel that interacts with external Ca^{2+}, disruption of which has allosteric implications across the pore domain to include altering distal Ca^{2+}-binding sites across the channel.

Despite visualizing multiple conformations of VSD2, it is worth considering the possibility that the mutations we used to trap such states may have induced instability in the domain. Neutralization of negatively charged residues could cause unwanted perturbations in the structure. Fortunately, we can rationalize our observations using the previously established electrophysiological recordings and those that we present in this manuscript. Hopefully, further structural and functional experiments will confirm and elaborate on our findings to complete our understanding of electrical activation in this channel.

Dickinson et al.
Molecular basis of multistep voltage activation in plant two-pore channel 1

PNAS | 7 of 10
https://doi.org/10.1073/pnas.2110936119

Using image processing, we determined multiple structures of sparsely populated states of a VGIC. These states reveal a mechanism for a multistep activation process. Further analysis will reveal whether similar processes occur in other VGICs, many of whose structures are currently limited to a single electrical state (18, 23, 36), in which elusive and dynamic processes may be responsible for the multitude of previously proposed, sometimes conflicting mechanisms of voltage activation.

Materials and Methods

Protein Expression and Purification. All AtTPC1 constructs were cloned into our 83nu yeast expression vector (41) that incorporates a carboxyl-terminal $10\times$ His tag preceded by a thrombin cleavage sequence. The plasmids were transformed into DSY5 *S. cerevisiae* and grown on synthetic complete media lacking histidine (SC-His⁻) plates. A single colony was used to inoculate a 100-mL starter culture of SC-His⁻ media and grown overnight at 30 °C. The starter culture was used to inoculate 750 mL SC-His⁻ media and grown overnight at 30 °C. A total of 250 mL Yeast Extract-Peptone-glycerol media was added to induce expression of TPC1 and grown overnight at 30 °C. All of the following steps were performed at 4 °C. Cells were harvested by centrifugation, resuspended in lysis buffer (50 mM Tris pH 7.5, 500 mM NaCl, 10% glycerol, 1 mM phenylmethylsulfonyl fluoride (PMSF), and one protease inhibitor tablet per 100 mL), and lysed by Emulsiflex. The lysate was centrifuged at 16,000 × g for 20 min to remove debris; then, the supernatant was centrifuged at 180,000 × g for 1 h to collect the membrane fraction. Membranes were resuspended in solubilization buffer (50 mM Tris pH 7.5, 200 mM NaCl, 1 mM PMSF, one protease inhibitor per 100 mL, and 1% β-dodecyl maltoside) such that the membrane mass to volume ratio is 1:20. The suspension was Dounce homogenized and nutated for 2 h. The suspension was centrifuged at 180,000 × g for 30 min to remove unsolubilized material. The supernatant was filtered through a 0.22-μm filter, and 20 mM imidazole was added along with 4 mL Ni^{2+}-NTA resin per 100 mL of lysate volume and allowed to batch bind for 4 to 5 h. The resin was collected on a (disposable) gravity column and washed with protein buffer (50 mM Tris pH 7.5, 200 mM NaCl, and 0.06% glycodiosgenin), first with 20 mM imidazole, then with 75 mM imidazole, and then in the absence of imidazole. The washed resin was resuspended in protein buffer, and 400 U thrombin was added for overnight, on-resin cleavage. The flow-through was collected, concentrated to 500 μL, and injected into a Superdex 200 increase 10/300 gel filtration column (GE Healthcare), preequilibrated in protein buffer supplemented either with 1 mM EDTA or $CaCl_2$. The peak fraction at ~10 mL (*SI Appendix*, Fig. S1) was collected and concentrated to ~5 mg mL⁻¹ for vitrification.

Microscopy. Freshly glow-discharged grids (300 mesh holey carbon Au Quantifoil R1.2/1.3) were used for vitrification in a Mark IV Vitrobot (FEI), using 100% relative humidity and 4-s blot time, and plunge frozen in liquid nitrogen–cooled ethane. The grids were loaded onto an FEI Titan Krios G3 electron microscope operating at 300 kV high tension, equipped with a K3 BioQuantum imaging system using a 20-eV energy slit. Imaging was performed in nanoprobe mode using a 50-μm C2 aperture using a ~1.3-μm parallel illuminated beam diameter and no objective aperture. The nominal magnification postenergy filter (EFTEM) magnification was 105,000×, corresponding to a calibrated super-resolution pixel size on the specimen of 0.4175 Å · pix⁻¹. The dose rate was 8 e⁻ · pix⁻¹ · s⁻¹ with a total exposure time of 5.9 s resulting in an accumulated fluence of 68 e⁻ · Å⁻² fractionated evenly across 117 frames, using correlated double sampling. Movies were acquired semiautomatedly with SerialEM (42) using 3 × 3 hole beam-image shift, using a nominal underfocus range of 0.7 to 1.5 μm with focus targeting once per nine shots. The movies were drift corrected and dose weighted using University of California, San Francisco (UCSF) MotionCor2 (43) and 2× Fourier binned to a pixel size of 0.835 Å · pix⁻¹.

Image Processing. For D454N-Ca^{2+}, 4,989 dose-weighted images (*SI Appendix*, Fig. S3) were imported into cryoSPARC version 2 (44), and contrast transfer function estimation was performed in patches. Micrographs with a CTF resolution worse than 5 Å were discarded. A total of 1,255,176 particles were picked using a Gaussian blob, extracted in 386-pixel boxes, and subjected to two-dimensional (2D) classification, resulting in 555,256 particles from the best classes. These particles were then used to calculate a C1 ab initio volume in cryoSPARC. The volume was aligned onto the cyclic symmetry axis using "relion_align_symmetry" and used as a reference for nonuniform refinement in cryoSPARC without imposition of symmetry. The map was then used as a reference for a three-class heterogeneous refinement in cryoSPARC, from which 140,438 particles from the best class (with apparent C2 symmetry) were retained. The

particles were subjected to nonuniform refinement with imposition of C2 symmetry while applying per-particle defocus refinement and per–beam-image shift group beam tilt refinement, yielding a 2.5-Å reconstruction by gold-standard Fourier shell correlation using a 0.143 threshold. Unfiltered, unmasked half maps from the refinement were subjected to both Deepemhancer (45) and density modification in Phenix (phenix.resolve_cryo_em) (46) for assistance with model building and atomic interpretation.

For D454N-EDTA, 8,629 dose-weighted images were imported into cryoSPARC version 2, and CTF estimation was performed in patches (*SI Appendix*, Fig. S4). A total of 1,447,101 particles were picked using a Gaussian blob and extracted in 386-pixel boxes. The particles were subjected to 2D classification from which 347,837 particles were selected from the best classes. These particles were then subjected to global angular refinement against the D454N-Ca^{2+} volume using NU-refinement with imposition of C2 symmetry. Although most of the volume was resolved to <3 Å resolution, VSD2 was essentially invisible. C2 symmetry expansion, followed by variability analysis in cryoSPARC with a focused mask over VSD2, demonstrated extensive heterogeneity in the domain, and numerous processing routes were employed to cluster the underlying conformational states; 3D classification into three classes showed two volumes, a high-resolution class similar in conformation to that in the Ca^{2+} structure, and a low-resolution class with an invisible VSD2. Refinement of the particles corresponding to the high-resolution class yielded a 2.7-Å reconstruction that appears identical to the Ca^{2+} structure (termed D454N-EDTA state I). In order to effectively separate the VSD2 conformations, the entire particle stack, before 3D classification, was exported to cisTEM (metadata was generated using csparc2star.py from Daniel Asarnow's pyem suite, and a single image stack generated using relion_preprocess), and a generous, cosine-edged mask comprising only half of the homodimer was calculated with relion_mask_create using a low-pass filtered D454N-Ca^{2+} volume as a template. The metadata were C2 symmetry–expanded using relion_particle_symmetry_expand and subjected to iterative rounds of 3D classification in cisTEM without alignment. Three distinct classes were isolated, displaying large conformational differences. The three classes are denoted states I through III, the first of which is the most similar to the D454N-Ca^{2+} structure and at highest resolution, and the third of which is the least similar and at lowest resolution (~8 Å resolution). Masked, resolution-limited refinement of state II yielded a promising map at 2.8 Å global resolution, with local resolution in the VSD2 region at ~3.5 Å. The particles were exported to cryoSPARC version 3 for C1 local refinement using a micelle-excluding mask. The half maps were subjected to postprocessing in Deepemhancer to assist with atomic modeling and interpretation.

For DDE-Ca^{2+}, 5,416 dose-weighted images were imported into cryoSPARC version 2, and CTF estimation was performed in patches (*SI Appendix*, Fig. S5). A total of 1,237,058 particles were picked using a Gaussian blob and extracted in 386-pixel boxes. The particles were subjected to 2D classification from which 257,025 particles were selected from the best classes. These particles were then subjected to global angular refinement against the D454N-Ca^{2+} volume using NU-refinement with imposition of C2 symmetry. The particle metadata was exported to star format and C2-symmetry expanded, and a single image stack was generated using relion_preprocess. A mask was calculated that encompasses only a single asymmetric unit and used in classification without alignment in cisTEM, which recovered classes nearly identical to those from the D454N-EDTA dataset. A total of 107,458 particles from the state II class were refined with local searches in C1. The half maps were subjected to modification in Deepemhancer, which better enabled modeling of VSD2.

Atomic Modeling. The atomic models were generated using the crystal structures of WT AtTPC1 as a reference [PDBs: 5DQQ (16) and 5E1J (22)] and manipulated in Coot (47), followed by iterative rounds of phenix.real_space_refine (46) and flexible fitting using Namdinator (48). All figures were prepared using UCSF Chimera (49).

Plant Cultivation. The TPC1 loss-of-function mutant *tpc1-2* from *Arabidopsis thaliana* (50) was cultivated in soil for 5 to 6 wk in a climate chamber with an 8-h light period and a light intensity of 150 μmol · m⁻² · s⁻¹. The temperature in the dark and light was adjusted to 16 °C and 22 °C, respectively, and the relative humidity was about 60%.

Cloning and Mutagenesis Procedure. Using the advanced uracil excision–based cloning technique (51, 52), the complementary DNA sequences coding for the AtTPC1 channel variants were cloned as carboxyl-terminal eGFP fusions (52) into the modified pSAT6-eGFP-C1 vector (GenBank AY818377.1), as essentially described by Dadacz-Narloch et al. (27). The AtTPC1 channel variants were under the control of the 35S promoter. Site-directed mutations were introduced in WT AtTPC1 following a modified USER (Uracil-Specific Excision

Reagent) fusion method as described by Dadacz-Narloch et al. (27). All channel mutants were verified by sequencing. Sequences of all used primers are provided in *SI Appendix*, Table S2.

Transient Protoplast Transformation. TPC1 channel variants were transiently expressed in mesophyll protoplasts according to a well-established protocol (53, 54). Briefly, for isolation of mesophyll protoplasts, the lower epidermis of the leaves was gently scrubbed with sandpaper before incubating the leaves for 3 h in the dark in the enzyme solution (1.5% cellulase R10, 0.4% macerozyme R10, 400 mM mannitol, 20 mM KCl, 20 mM MES (4-morpholineethanesulfonic acid), 10 mM $CaCl_2$, and 0.1% BSA (Albumin, Fraction V), pH 5.7 adjusted with Tris). The suspension was then filtered and washed through a 50-μm nylon mesh with 30 to 40 mL W5 buffer (154 mM NaCl, 125 mM $CaCl_2$, 5 mM KCl, 5 mM glucose, and 2 mM MES, pH 5.7 adjusted with Tris) and centrifuged at 100 × g for 2 min without acceleration or brake at 4 °C. After removing the supernatant, the enriched protoplasts were incubated on ice for 30 min in W5 to settle at the bottom of the tube. The supernatant was replaced by 5 to 8 mL MMg (Mannitol/Mg) solution (0.4 M mannitol, 15 mM $MgCl_2$ and 4 mM MES pH 5.7) to obtain about 2×10^5 protoplasts per milliliter MMG. A 200-μL protoplast suspension was gently mixed with 20 μg plasmid DNA and 220 μL PEG (polyethylene glycol) solution (2 g PEG 4000, 1.5 mL H_2O, 1.25 mL mannitol [800 mM], and 0.5 mL $CaCl_2$ [1 M]) and incubated for 15 min at room temperature. To stop the reaction, W5 (440 μL) was added to the protoplast suspension. After shaking the tube gently for few seconds, W5 (880 μL) was added for further dilution. Following centrifugation at 100 × g for 1 min, the supernatant was removed, and the protoplasts were resuspended and stored in 1.5 mL W5 buffer (plus 50 μg · mL^{-1} ampicillin) in the dark and at room temperature for 2 d.

Fluorescence Imaging. To image the correct vacuolar membrane targeting of the TPC1 constructs, the GFP fluorescence signal of transformed protoplasts and vacuoles released therefrom were detected using a confocal laser scanning microscope (TCS SP5, Leica) (55).

Patch-Clamp Experiments. A total of 2 d after transformation, an aliquot of the protoplast suspension (50 μL) was transferred to the patch-clamp recording chamber, and the vacuole-releasing (VR) solution was added [250 to 400 μL VR solution, modified in comparison to that of Lagostena et al. (56)]. The VR solution was composed of 100 mM malic acid, 155 mM N-methyl-D-glucamine, 5 mM EGTA, 3 mM $MgCl_2$, and 10 mM Hepes/Tris pH 7.5 and adjusted to 450 mOsmol·· kg^{-1} with D-sorbitol. After the whole-vacuole patch-clamp configuration was established with fluorescent vacuoles harboring GFP-tagged TPC1 channels, the VR solution was replaced by the standard bath medium. The bath solution consisted of 150 mM KCl, 1 mM $CaCl_2$, and 10 mM Hepes (pH 7.5/Tris) and was adjusted with D-sorbitol to an osmolality of 520 mOsmol·· kg^{-1}. Patch pipettes with a resistance of 1.5 to 3.9 MΩ were filled with one of two pipette solutions. Both pipette solutions were composed of 150 mM KCl, 2 mM $MgCl_2$, and 10 mM Hepes (pH 7.5/Tris) and adjusted with D-sorbitol to an osmolality 500 mOsmol·· kg^{-1}. One of the pipette solutions additionally contained 0.1 mM EGTA to adjust nominal 0 mM Ca^{2+} (https://somapp.ucdmc.ucdavis.edu/pharmacology/bers/maxchelator/webmaxc/webmaxcE.htm), while 10 mM $CaCl_2$ was added to the other. The patch pipettes were made of thin-wall borosilicate glass capillaries (1.5 outer diameter × 1.17 inner diameter; Harvard glass capillaries GC150T-10, Harvard Apparatus). The inner wall of the glass capillaries was coated with Sigmacote (Sigma-Aldrich) before the capillaries were drawn with a two-stage puller (PC-10, Narishige Group). Using a microforge (L/MCPZ 101, List Medical-Elektronic), the pulled glass pipettes were coated near the tip with Sylgard (184 Silicone elastomer Kit, Dow Corning Corporation), and then the tips were fire polished. Current recordings were performed at a sampling rate of 150 μs and a filter frequency at 3 kHz using an EPC800 patch-clamp amplifier (HEKA Electronic). Data acquisition was carried out with the software program Pulse (HEKA Electronic). For the patch-clamp experiments, individual vacuoles with a membrane capacitance of 31 to 69 pF were used to study the channel variants under different luminal Ca^{2+} conditions. According to the voltage convention for endomembranes (57), the membrane potential is given for the cytosolic side of the vacuole membrane, while the membrane potential at the luminal side is set to zero.

The currents were measured in response to voltage pulses (1 s) in the range of −80 mV to +110 mV applied in 10-mV increments from a holding voltage of −60 mV. The steady-state current amplitudes (I_{ss}) were determined at the end of the current responses to the voltage pulses and normalized to the compensated membrane capacitance (C_m) of the investigated vacuole, which was used as a measure for the vacuole membrane surface. For conductance/voltage curves [$G/G_{max}(V)$], instantaneous tail currents (I_t) were determined from tail currents, which were recorded at −60 mV after the vacuole membrane was clamped to voltage prepulses (1 s) in the range of −80 mV to +110 mV. Following a linear kinetic three-state model for the plant TPC1 channel [$C_2 \rightleftharpoons C_1 \rightleftharpoons O$, with two closed states $C_{1/2}$ and one open state O (58)], the tail currents I_t were plotted against the respective prepulse voltages and fitted with a double Boltzmann equation as follows:

$$I_t(V) = I_{max} \cdot \frac{1}{1 + \exp\left(-z_1 \cdot \frac{V - V_1}{k_B \cdot T}\right) \cdot \left(1 + \exp\left(-z_2 \cdot \frac{V - V_2}{k_B \cdot T}\right)\right)},$$

with $k_B \cdot T = 25.26$ mV at room temperature. V_1 and V_2 give the half-activation voltages for the $C_1 \rightleftharpoons O$ and the $C_2 \rightleftharpoons C_1$ transitions, respectively. z_1 and z_2 represent the apparent equivalent gating charges of these transitions.

The tail currents and the fits were then normalized to the maximal predicted currents (I_{max}) of the best Boltzmann fit to obtain the normalized conductance–voltage curves [$G/G_{max}(V) = I_t/I_{max}(V)$]. Data were analyzed with the software programs pulse (HEKA Electronic) and Igor Pro-6.11 (Wavemetrics Inc.).

Statistical Analysis. Data are presented as means ± SE. Significant differences in $V_{1/2}$ values under 0 mM luminal Ca^{2+} conditions were analyzed with one-way ANOVA followed by the Dunnett's post hoc comparison test. To perform the statistical analysis (one-way ANOVA with Dunnett's post hoc comparison test) of the Ca^{2+}-induced shift in the $V_{1/2}$ values, the means of the V_1 and V_2 values determined in the absence of luminal Ca^{2+} were subtracted from the individual V_1 and V_2 values, respectively, derived under 10 mM luminal Ca^{2+} conditions. Levene's test and Shapiro–Wilk test confirmed assumed equal variance and normality of the data points. Significant differences in z_1 and z_2 values at each Ca^{2+} condition were analyzed with one-way ANOVA followed by Dunnett's post hoc comparison test. Significance of Ca^{2+}-induced changes in $z_{1/2}$ values were tested with Student's t test. Sample size was not predetermined; under consideration of technical feasibility, we conducted a minimum of independent patch-clamp experiments on individual vacuoles per each channel construct and luminal Ca^{2+} condition. Statistical analysis was carried out with SPSS 2020 (IBM).

Data Availability. The unfiltered and unmasked half maps, unsharpened volumes, postprocessed volumes, and atomic models are available in the Electron Microscopy Data Bank and PDB under accession nos. PDBID-7TBG and EMD-25798 (AtTPC1 D454N-Ca^{2+}); PDBID-7TDF and EMD-25827 (AtTPC1 D454N-EDTA state I); PDBID-7TDD and EMD-25825 (AtTPC1 D454N-EDTA state II); and PDBID-7TDE and EMD-25826 (AtTPC1 DDE-Ca^{2+}). The atomic coordinates for the structures are available in the PDB. All plasmids are available upon request.

1. W. A. Catterall, G. Wisedchaisri, N. Zheng, The chemical basis for electrical signaling. *Nat. Chem. Biol.* **13**, 455–463 (2017).
2. B. Hille, *Ionic Channels of Excitable Membranes* (Sinauer, Sunderland, Massachusetts, 1991).
3. A. L. Hodgkin, A. F. Huxley, A quantitative description of membrane current and its application to conduction and excitation in nerve. *J. Physiol.* **117**, 500–544 (1952).
4. F. Bezanilla, How membrane proteins sense voltage. *Nat. Rev. Mol. Cell Biol.* **9**, 323–332 (2008).
5. R. Hedrich, Ion channels in plants. *Physiol. Rev.* **92**, 1777–1811 (2012).
6. Y. Wang et al., Cytosolic Ca^{2+} signals enhance the vacuolar ion conductivity of bulging Arabidopsis root hair cells. *Mol. Plant* **8**, 1665–1674 (2015).
7. H. Xu, D. Ren, Lysosomal physiology. *Annu. Rev. Physiol.* **77**, 57–80 (2015).
8. F. Bezanilla, Gating currents. *J. Gen. Physiol.* **150**, 911–932 (2018).
9. J. Payandeh, D. L. Minor, Jr, Bacterial voltage-gated sodium channels (BacNaVs) from the soil, sea, and salt lakes enlighten molecular mechanisms of electrical signaling and pharmacology in the brain and heart. *J. Mol. Biol.* **427**, 3–30 (2015).

Dickinson et al.
Molecular basis of multistep voltage activation in plant two-pore channel 1

PNAS | 9 of 10
https://doi.org/10.1073/pnas.2110936119

PLANT BIOLOGY

BIOPHYSICS AND COMPUTATIONAL BIOLOGY

10. G. Dai, T. K. Aman, F. DiMaio, W. N. Zagotta, The HCN channel voltage sensor undergoes a large downward motion during hyperpolarization. *Nat. Struct. Mol. Biol.* **26**, 686–694 (2019).

11. B. Chanda, O. K. Asamoah, R. Blunck, B. Roux, F. Bezanilla, Gating charge displacement in voltage-gated ion channels involves limited transmembrane movement. *Nature* **436**, 852–856 (2005).

12. K. S. Glauner, L. M. Mannuzzu, C. S. Gandhi, E. Y. Isacoff, Spectroscopic mapping of voltage sensor movement in the Shaker potassium channel. *Nature* **402**, 813–817 (1999).

13. H. Xu *et al.*, Structural basis of Nav1.7 inhibition by a gating-modifier spider toxin. *Cell* **176**, 1238–1239 (2019).

14. T. Clairfeuille *et al.*, Structural basis of α-scorpion toxin action on Na$_v$ channels. *Science* **363**, eaav8573 (2019).

15. G. Wisedchaisri *et al.*, Resting-state structure and gating mechanism of a voltage-gated sodium channel. *Cell* **178**, 993–1003.e12 (2019).

16. A. F. Kintzer, R. M. Stroud, Structure, inhibition and regulation of two-pore channel TPC1 from *Arabidopsis thaliana*. *Nature* **531**, 258–262 (2016).

17. A. F. Kintzer *et al.*, Structural basis for activation of voltage sensor domains in an ion channel TPC1. *Proc. Natl. Acad. Sci. U.S.A.* **115**, E9095–E9104 (2018).

18. M. S. Dickinson, A. Myasnikov, N. Eriksen, N. Poweleit, R. M. Stroud, Resting state structure of the hyperdepolarization activated two-pore channel 3. *Proc. Natl. Acad. Sci. U.S.A.* **117**, 1988–1993 (2020).

19. A. F. Kintzer, R. M. Stroud, On the structure and mechanism of two-pore channels. *FEBS J.* **285**, 233–243 (2018).

20. R. Hedrich, T. D. Mueller, D. Becker, I. Marten, Structure and function of TPC1 vacuole SV channel gains shape. *Mol. Plant* **11**, 764–775 (2018).

21. R. Hedrich, I. Marten, TPC1-SV channels gain shape. *Mol. Plant* **4**, 428–441 (2011).

22. J. Guo *et al.*, Structure of the voltage-gated two-pore channel TPC1 from *Arabidopsis thaliana*. *Nature* **531**, 196–201 (2016).

23. J. She *et al.*, Structural mechanisms of phospholipid activation of the human TPC2 channel. *eLife* **8**, e45222 (2019).

24. D. Jaślan *et al.*, Gating of the two-pore cation channel AtTPC1 in the plant vacuole is based on a single voltage-sensing domain. *Plant Biol.* **18**, 750–760 (2016).

25. D. Jaślan *et al.*, Voltage-dependent gating of SV channel TPC1 confers vacuole excitability. *Nat. Commun.* **10**, 2659 (2019).

26. D. Beyhl *et al.*, The fou2 mutation in the major vacuolar cation channel TPC1 confers tolerance to inhibitory luminal calcium. *Plant J.* **58**, 715–723 (2009).

27. B. Dadacz-Narloch *et al.*, A novel calcium binding site in the slow vacuolar cation channel TPC1 senses luminal calcium levels. *Plant Cell* **23**, 2696–2707 (2011).

28. J. Guo, W. Zeng, Y. Jiang, Tuning the ion selectivity of two-pore channels. *Proc. Natl. Acad. Sci. U.S.A.* **114**, 1009–1014 (2017).

29. G. Bonaventure *et al.*, A gain-of-function allele of TPC1 activates oxylipin biogenesis after leaf wounding in Arabidopsis. *Plant J.* **49**, 889–898 (2007).

30. A. Lenglet *et al.*, Control of basal jasmonate signalling and defence through modulation of intracellular cation flux capacity. *New Phytol.* **216**, 1161–1169 (2017).

31. R. Hedrich *et al.*, General mechanisms for solute transport across the tonoplast of plant vacuoles: a patch-clamp survey of ion channels and proton pumps. *Bot. Acta* **101**, 7–13 (1988).

32. C. A. Ahern, J. Payandeh, F. Bosmans, B. Chanda, The hitchhiker's guide to the voltage-gated sodium channel galaxy. *J. Gen. Physiol.* **147**, 1–24 (2016).

33. X. Zhang, N. Yan, The conformational shifts of the voltage sensing domains between Na$_v$Rh and Na$_v$Ab. *Cell Res.* **23**, 444–447 (2013).

34. J. Payandeh, T. M. Gamal El-Din, T. Scheuer, N. Zheng, W. A. Catterall, Crystal structure of a voltage-gated sodium channel in two potentially inactivated states. *Nature* **486**, 135–139 (2012).

35. X. Zhang *et al.*, Crystal structure of an orthologue of the NaChBac voltage-gated sodium channel. *Nature* **486**, 130–134 (2012).

36. J. She *et al.*, Structural insights into the voltage and phospholipid activation of the mammalian TPC1 channel. *Nature* **556**, 130–134 (2018).

37. T. Dudev, C. Lim, Ion selectivity strategies of sodium channel selectivity filters. *Acc. Chem. Res.* **47**, 3580–3587 (2014).

38. T. Dudev, C. Lim, Evolution of eukaryotic ion channels: Principles underlying the conversion of Ca^{2+}-selective to Na$^+$-selective channels. *J. Am. Chem. Soc.* **136**, 3553–3559 (2014).

39. E. Gouaux, R. Mackinnon, Principles of selective ion transport in channels and pumps. *Science* **310**, 1461–1465 (2005).

40. H. Zheng *et al.*, Validation of metal-binding sites in macromolecular structures with the CheckMyMetal web server. *Nat. Protoc.* **9**, 156–170 (2014).

41. M. Li *et al.*, Selecting optimum eukaryotic integral membrane proteins for structure determination by rapid expression and solubilization screening. *J. Mol. Biol.* **385**, 820–830 (2009).

42. M. Schorb, I. Haberbosch, W. J. H. Hagen, Y. Schwab, D. N. Mastronarde, Software tools for automated transmission electron microscopy. *Nat. Methods* **16**, 471–477 (2019).

43. S. Q. Zheng *et al.*, MotionCor2: Anisotropic correction of beam-induced motion for improved cryo-electron microscopy. *Nat. Methods* **14**, 331–332 (2017).

44. A. Punjani, J. L. Rubinstein, D. J. Fleet, M. A. Brubaker, cryoSPARC: Algorithms for rapid unsupervised cryo-EM structure determination. *Nat. Methods* **14**, 290–296 (2017).

45. R. Sanchez *et al.*, DeepEMhancer: A deep learning solution for cryo-EM volume postprocessing. *Commun. Biol.* **4**, 1–8 (2021).

46. D. Liebschner *et al.*, Macromolecular structure determination using X-rays, neutrons and electrons: Recent developments in Phenix. *Acta Crystallogr. D Struct. Biol.* **75**, 861–877 (2019).

47. P. Emsley, B. Lohkamp, W. G. Scott, K. Cowtan, Features and development of Coot. *Acta Crystallogr. D Biol. Crystallogr.* **66**, 486–501 (2010).

48. R. T. Kidmose *et al.*, *Namdinator* - automatic molecular dynamics flexible fitting of structural models into cryo-EM and crystallography experimental maps. *IUCrJ* **6**, 526–531 (2019).

49. E. F. Pettersen *et al.*, UCSF Chimera–a visualization system for exploratory research and analysis. *J. Comput. Chem.* **25**, 1605–1612 (2004).

50. E. Peiter *et al.*, The vacuolar Ca^{2+}-activated channel TPC1 regulates germination and stomatal movement. *Nature* **434**, 404–408 (2005).

51. H. H. Nour-Eldin, B. G. Hansen, M. H. H. Nørholm, J. K. Jensen, B. A. Halkier, Advancing uracil-excision based cloning towards an ideal technique for cloning PCR fragments. *Nucleic Acids Res.* **34**, e122 (2006).

52. G. Zhang, V. Gurtu, S. R. Kain, An enhanced green fluorescent protein allows sensitive detection of gene transfer in mammalian cells. *Biochem. Biophys. Res. Commun.* **227**, 707–711 (1996).

53. J. Sheen, A transient expression assay using Arabidopsis mesophyll protoplasts. http://genetics.mgh.harvard.edu/sheenweb/protocols/AtprotoRL04.pdf. Accessed 8 May 2016.

54. S.-D. Yoo, Y.-H. Cho, J. Sheen, Arabidopsis mesophyll protoplasts: A versatile cell system for transient gene expression analysis. *Nat. Protoc.* **2**, 1565–1572 (2007).

55. B. Dadacz-Narloch *et al.*, On the cellular site of two-pore channel TPC1 action in the Poaceae. *New Phytol.* **200**, 663–674 (2013).

56. L. Lagostena, M. Festa, M. Pusch, A. Carpaneto, The human two-pore channel 1 is modulated by cytosolic and luminal calcium. *Sci. Rep.* **7**, 43900 (2017).

57. A. Bertl *et al.*, Electrical measurements on endomembranes. *Science* **258**, 873–874 (1992).

58. I. I. Pottosin, M. Martínez-Estévez, O. R. Dobrovinskaya, J. Muñiz, G. Schönknecht, Mechanism of luminal Ca^{2+} and Mg^{2+} action on the vacuolar slowly activating channels. *Planta* **219**, 1057–1070 (2004).